DISPERSION (ELECTROSTATIC/MECHANICAL) AND FUEL PROPERTIES EFFECTS ON SOOT PROPENSITY IN CLUSTERS OF DROPS

J. Bellan and K. Harstad

Jet Propulsion Laboratory

California Institute of Technology

4800 Oak Grove Drive

Pasadena, CA. 91109

Abstract

Soot propensity is studied numerically for an initially binary size, axisymmetric cluster of evaporating drops by defining it as the propensity for nucleation reactions to occur; the study does not address physical or chemical processes ensuing after soot nucleation. The relative magnitude of the fuel vapor partial density is taken as an indication of the soot nucleation magnitude; thus, the effect of drop dispersion on soot (precursor) formation is isolated from that of soot production resulting from formation/destruction by oxidation. The cluster is embedded in an inviscid vortex and exchanges mass, momentum, species and energy with its surroundings. The vertical motion disperses the drops and the initial cluster evolves into a

cylindrical shell with an inner and outer boundary. Additional to the forces resulting from the vertical motion, an electrostatic force acts on the cluster when the drops are charged; in this sit uat ion, the drops might become small enough to reach the Rayleigh limit. Analysis of the results shows that for uncharged drops, their motion is primarily determined by centrifugation whereas for charged drops the electrostatic dispersion becomes the dominant influence in the outer part of the cluster. In the range of parameters investigated, mechanical dispersion cannot rival electrostatically induced dispersion for decreasing the fuel vapor partial density. An additional feature of drop charging is the maintenance of a finite slip velocity in the outer part of the cluster, thereby compounding the advantage of increased dispersion to enhanced evaporation. The results also show that mechanical dispersion combined with electrostatic dispersion does not have a substantial advantage over electrostatic dispersion alone. For uncharged drops it has been found that the latent heat governs soot propensity at small drop dispersion whereas the liquid density becomes increasingly important with increasing drop dispersion. Drop charging does not affect the influence of fuel properties on soot propensity.

1 Introduction

Soot produced by burning liquid fuel sprays has been a problem both in the automotive industry and in missile liquid propulsion. However, whereas soot formation from gaseous fuels has been studied extensively both in the context of premixed and diffusion flames [1], definitive studies are still lacking for sprays. Spray flames are in many respects similar to gas diffusion flames, however, soot production resulting from spray combustion involves several additional time scales when compared to gaseous flames; the drop heating time, the liquid evaporation time and the drop dispersion time are new time scales interacting with the mixing and chemical times encountered in gaseous diffusion

flames.

Single drop experiments can reveal the interaction of the heating and evaporation times with the mixing and chemical times. Early experiments on soot produced by burning, isolated drops were performed by Kadota et al. [2], Nakanishi et al. [3], and by Kadota and Hiroyasu [4] to study respectively the effects of pressure, convection and temperature, and fuel additives such as ethanol and n-heptane. It was found that sooting decreases with increasing air velocity; that the amount of soot increases with pressure; that the composition of the drop surroundings, particularly the oxygen concentration, has an important influence on the ultimate amount of soot. produced; that soot production increases with the C/H ratio; and that larger drops produce relatively more soot. Within the context of soot reduction associated with alcohol blending and water emulsions, Randolph and Law [5] observed the gasification of freely-falling drops and determined that the causes of soot reduction were both the dilution of the fuel composition by the non-sooting components and the reduction in the flame temperature associated with the reduction in the heat of combustion. The influence of the flame temperature on soot formation from single toluene drops was also investigated by Lee et al. [6]. Their experiment was performed with single suspended toluene drops and it was found that under reduced pressure (from atmospheric) the soot reduction resulted from the combined effect of the flame temperature and Grashof number reductions. Recently, Law [7] has experimentally studied the sooting behavior of isolated liquid drops and showed that a class of very promising high-energy density fuels for missile propulsion is unfortunately very prone to soot formation.

Even when individual fuel drops burn without forming substantial amounts of soot, the same fuel may form considerably larger amounts of soot when burning as a spray. This is due to the possible formation of gaseous pockets containing large concentrations of fuel vapor in which nucleation

reactions are initiated. Therefore, drop dispersion is a crucial aspect of soot control in sprays.

Although sooting from spray flames has been mainly studied in the context of Diesel engines [8], the relationship between drop dispersion and soot formation has been specifically investigated by Sangiovanni and Liscinsky [9] who observed streams of burning drops and found that the soot emission index decreases monotonically with the spacing between drops. The observations yielded consistent trends for several oxygen mass fractions in the surrounding gas and for a variety of fuels; however, no connection was made between the fuel thermophysical properties and soot production. Since in Sangiovanni and Liscinsky's study [9] it is only the effect of drop spacing in a single direction that has been investigated, those results underestimate the benefit of drop dispersion in a real spray where a drop is surrounded by other drops in all directions. The numerical results of Bellan and Harstad [10] obtained for enhanced, electrostatically induced dispersion of evaporating drops, concur with the experimental results of Sangiovanni and Liscinsky [9]. They show that both the evaporated fuel interstitial mass fraction, Y_{Fi}, and the interstitial gas density, ρ_{gi}, decrease for evaporating, electrostatically charged drops when compared to uncharged drops. Since formation of soot precursors through nucleation reactions is directly associated with the partial density of the fuel in the gas phase [12], a reduction in both Y_{Fi} and ρ_{gi} implies a strong reduction in the partial density of the fuel vapor, $Y_{Fi}\rho_{gi}$, and is thus an indication of reduced soot nucleation. In this study wc consider that soot nucleation is the indication of soot propensity. Thus, the present study is devoted to identifying fuel properties and fluid mechanical aspects related to soot propensity, but does not consider physical or chemical aspects related to the evolving soot concentration once the soot precursors have been formed.

The study of Bellan and Harstad [10] was conducted for vortex-embedded clrop-clusters of three representative high-energy fuels. These representative fuels are benzvalene (BV), C_6H_6; quadricy-

clane (QUAD), C_7H_8; and dihydrobenzvalene (DHBV), C_6H_8. The properties of these fuels have been calculated by Bellan [11] and arc reproduced in Table 1. An inspection of the fuel properties shows that: (1) BV and QUAD have identical latent heats (to t he accuracy of the properties calculation), (2) BV and DHBV have very similar molecular weights and normal boiling points, and (3) QUAD and DHBV have identical liquid densities (to the accuracy of the properties calculation). The results of Bellan and Harstad [10] show that the latent heat is a fuel property that governs the soot propensity for otherwise identical initial air/fuel mass ratio and drop and gas initial conditions; thus, among the three fuels, DHBV is most prone to soot formation (because of its smaller latent heat). The importance of the latent heat is due to its determining influence on the evaporation time when the drops are in close proximity [13] in contrast to the boiling point governing the evaporation time when the drops are far apart [13]. Significantly, Bellan and Harstad [10] found that electrostatic dispersion has most impact in reducing soot nucleation for DHBV drops. Bellan and Harstad [10] also show that even a small amount, of electrostatic charge (25% of the maximum possible with the spray triode [14]) has a considerable effect upon the value of $Y_{Fi}\rho_{gi}$, and that the largest changes are obtained by charging (i.e. from 0% to 25% of the maximum charge) rather than by increasing the initial charge (to 50% or 75% of the maximum charge).

Although results from both isolated drop [3] and spray studies [8] show a reduction of collected soot with increased air velocity, it is unclear if this reduction is due to soot produced being further oxidized (soot production as a result of formation/destruction reactions) or to the inherent reduction in soot formation, or to both effects. Experiments to discriminate between the two situations are difficult to perform since one would have to arrest soot growth and oxidation while allowing soot precursor formation; experiments in absence of oxygen would eliminate oxidation reactions but would still allow soot growth. However, numerical studies can isolate the effect of soot precursor

formation; this is one of the goals of this study. (Previous results [10] indicate that soot precursor formation is indeed reduced by drop dispersion.) In the present investigation we also wish to determine what level of mechanical dispersion could affect the drops to the same degree as the electrostatic dispersion, and want to explore the possibility of combining electrostatic with fluid mechanical dispersion (e.g. creation of turbulent vertical structures) in order to further mitigate soot formation. In addition, we want to determine which of the fuel properties or operating conditions related to drop dynamics are most influential on soot propensity; because of the differences and similarities in the fuel properties as explained above, BV, DHBV and QUAD are ideally suited for this comparative study. In Section 2, we describe the mathematical model; Section 3 is devoted to the discussion of the results. Finally, in Section 4 we present our conclusions.

2 Model

The model of the evaporating cluster of drops in an inviscid vortex has been described in detail in Harstad and Bellan [15], whereas the model of electrostatic dispersion of polydisperse collections of drops has been derived by Bellan and Harstad [10]; only a brief exposition of the two models is presented below and the reader is referred to [15], [10] for details of the models and solution technique for the conservation equations.

The physical configuration of the cluster of drops embedded into an axisymmetric vortex is depicted in Fig. 1 for an initial binary drop size distribution. Each drop initial-size-class distribution is followed in its own system of coordinates moving with the drops, r_j, where j denotes the initial-size-class, whereas the gas is followed in its own system of coordinates, r_c. The cluster volume is bounded by surfaces which are the statistical envelopes of the outermost (R_c) and innermost (R_{in})

drops. The gas Reynolds number is defined as $Re = u_g R_c/\mu_g$ where u_g is gas velocity, R_c is cluster radius, and μ_g is gas viscosity; typically $Re \sim O(10^4)$ so that the vortex is inviscid. The drop Reynolds number is defined as $Re_{dj} = u_{sj} R_j/\mu_g$ where $\vec{u}_{sj} = \vec{u}_{dj} - \vec{u}_g$ is the local slip velocity between phases, $\vec{u}_{dj}$ is the drop velocity and R_j is the drop radius. Initially, $Re_{dj} \sim$ O(1) – 0(10) so that a drag force resulting from shape-drag, friction and drop evaporation causes interaction between drops and gas.

The concept of 'sphere of influence' [16] around each drop is used to model heat and mass transfer within and around each drop. Here, we define the radius of the sphere of influence, R_i, statistically using

$$4\pi R_i^3 n/3 \equiv PF \tag{1}$$

where n = $\sum_{j=1}^{JT} n_j$ is the total drop number density, JT is the total number Of initial-size classes, n_j is the drop number density for initial-size-class j, and PF = 0.74 is the packing factor [16]. With this definition, the class j evaporation rate $\dot{m}_{dj}$ can be calculated for each R_j using a Previously derived model [17].

The ratio of the Kolmogorov scale η_K to R_j is estimated from $Re^{-0.75} R_c/R_j$ since $\eta_K/R_c \sim Re^{-0.75}$. For the characteristic values $\|\vec{u}_g\| = 10^3$cm/s, μ_g = 4.2 x 10^{-4}g/(cm s), R_c = 2 cm and R_j = 2 x 10^{-3} cm, one obtains $\eta_K/R_j \sim O(1)$. Since in the very dense configuration $R_i/R_j \sim O(10)$, there are many Kolmogorov-t ype eddies between adjacent drops.

2.1 **Conservation equations for the drops**

For each initial-size class j the drop conservation are:

$$\partial n_j/\partial t + [\partial(r n_j u_{drj})/\partial r]/r = 0 \qquad (2)$$

$$dr_j/dt = u_{drj} \qquad (3)$$

$$du_{drj}/dt = [u_{d\theta j}]^2/r_j - \nu_{sj}[u_{drj} - u_{gr}(r_j)] + D_{dTj}\{\partial\{[\partial(r u_{drj})/\partial r]/r]\}/\partial r$$
$$+\partial[\ln(n_j/n_j^0)]/\partial r \times \partial u_{drj}/\partial r\} - (1/\rho_l)\,[\sum_j n_j(\nu_{sj} m_{dj} - \dot{m}_{dj})u_{srj}]/(1 - f_{vl}) + q_{dj}E_r/m_{dj} \qquad (4)$$

$$d(r_j u_{d\theta j})/dt = -\nu_{sj}[r_j u_{d\theta j} - r_j u_{g\theta}] \qquad (5)$$

where ρ_l is the liquid density, $\nu_{sj} \equiv \rho_g A_{dj} C_{Dj} \|u_{sj}\|/(2m_{dj})$ is a rate associated with drag, A_{dj} is the drop transverse area, C_{Dj} is the drag coefficient [assumed to have the same dependence upon Re_{dj} and evaporative blowing parameter as in Bellan and Harstad [18] and Cliffe and Lever [19]], m_{dj} is the drop mass, the liquid volume fraction is $f_{vl} \equiv (\sum_j n_j m_{dj})/\rho_l$, subscripts r and θ refer to radial and tangential coordinates, and u_{drj} includes the diffusive velocity. These equations hold between $r_{in,j}$ and $r_{out,j}$, respectively the inner and outer radius of distribution j. The right hand side of Eq. 4 represents the effect of drop turbulence which is modeled as a diffusive process with $D_{dTj} = A_T \nu_{sj}(r_j)^2$ where $A_T \equiv C_T/\mathrm{Pr}_g$; $C_T = 0.05$ is a constant associated with the scaling model based upon the Prandtl mixing length approach. The influence of the value of C_T upon the solution has been studied in [15].

The last term in Eq. 4 is the change of the radial force on a drop of initial-size class j due to an electrostatic charge q_{dj}, where E_r is the radial electric field. The value of E_r is found from Poisson's equation

$$p = \rho \tilde{R} T_g \tag{13}$$

where Y_i is the mass fraction of species i (F denotes the fuel), $D_T = (\mu_g + \mu_T)/(\rho_g Sc_g)$ is calculated by prescribing the gas Schmidt number Sc_g, $h_g = C_{pg} T_g$ is the enthalpy, $\rho_g h_g = \gamma p/(\gamma - 1)$, γ is the ratio of the heat capacities, C_p is the specific heat capacity at constant pressure, k_g is the conductivity calculated from $k_g = (\mu_g + \mu_T) C_{pg}/\mathrm{Pr}_g$ by prescribing Pr_g, and $\triangle h_{evap}$ is the heat transferred to the drop from the gas per unit mass of evaporated fuel. The third and fourth terms on the right hand side of Eq. 12 show how incoming fuel vapor changes gas thermal and kinetic energies respectively, while the last term gives viscous dissipation from drag. The gas constant is $\tilde{R} = R_u \sum_i Y_i/w_i$, where R_u is the universal gas constant and w_i is the molecular weight. The gas Lewis number is taken to be unity ($Sc_g = \mathrm{Pr}_g$), an accurate assumption for a gas.

2.3 **Boundary conditions**

The cluster boundaries (through which mass, species, momentum and energy are exchanged with the cluster surroundings) are the statistical envelopes of the inner and outer drops; they are defined by $R_{in} = \min_j (r_{in,j})$ and $R_c = \max_j (r_{out,j})$ where $r_{in,j}$ and $r_{out,j}$ are initially defined for all $j's$. Three regions are thus identified: (1) an inner drop-free region where the gas conservation equations are solved, (2) the cluster region where both gas and drop conservation equations are solved, and (3) the outer gas region where heat, mass and species satisfy convective-diffusive equations. To simulate the exchange processes though the boundaries (which appear to the surrounding gas as 'porous' since the cluster cannot be easily penetrated), a Nusselt number approach is utilized together with a heat/mass similarity assumption. The correlation $Nu_c = 1 + \mathrm{Cl}\, \mathrm{Pr}_g Re_c$ is used where

$Re_c = [\rho_g r_c \max(0, u_{cr} - u_{gr})/(\mu_g + \mu_{T'})]_{r=R_c}$ is the effective Reynolds number. The power exponent of Pr_g and Re_c is unity in the Nu_c correlation so that for $C_1 = 1$ the transfer between cluster and ambient is an engulfing/emitting process: if $u_{cr} = (\sum_j n_j m_{dj} u_{drj})/(\sum_j n_j m_{dj}) > u_{gr}$, the cluster engulfs gas at a rate proportional to $[r_c \rho_g (u_m - u_{gr})]_{r=R_c}$; if $u_{gr} > u_{cr}$ the cluster emits gas and only weak diffusion couples it to the surrounding gas. In all the present calculations Cl = 0.50; the effect of Cl upon the solution has been studied elsewhere[15]. Consistent with the similarity assumption $Sc_g = \mathrm{Pr}_g$, the boundary condition for the evaporating species is

$$(r\partial Y_F/\partial r)_{r=R_c} = Nu_c(Y_{F\infty} - Y_{F,r=R_c}). \qquad (14)$$

At the inner cluster boundary, $\partial\Gamma/\partial r = 0$, where $\Gamma' = Y_F$ or $\Gamma = T'_i$. At the vortex center (taken to be an infinitesimally small radial distance to avoid singularities), the gradients of velocities and all dependent variables gradients vanish. In all the present calculations there is no vapor of the evaporating compound in the far field and $T_{g\infty}(t) = T^0_{g\infty}$ [1 + $t/(6 \times 10{-}3)$] in order to simulate the passage of the vortex through an increasing temperature region; $T^0_{gi} = T^0_{g\infty}$. Similarly, $Y^0_{Fi} = Y^0_{F\infty}$.

2.4 **Initial conditions**

The spatial dependence of n^0_j or the initial air/liquid mass ratio, Φ^0, can be prescribed to yield an initial drop count [15]. Additional initial dependent variables to be prescribed are the drop temperature, T_{ds}, gas pressure and temperature; cluster radius; irrotational component, $A^0_{g\theta}$ and $A^0_{d\theta}$, and solid body rotation component, $B^0_{g\theta}$ and $B^0_{d\theta}$, of the gas and drop tangential velocities, respectively $u^0_{g\theta} = A^0_{g\theta}/r^0 + B^0_{g\theta} r^0$ and $u^0_{d\theta} = A^0_{d\theta}/r^0 + B^0_{d\theta} r^0$. u^0_{gr} *is* calculated from the gas energy equation and $u^0_{dr} = 0$. The electrostatic charge and initial properties of gas (air) and liquid are also

prescribed.

2.5 The Rayleigh limit

Both Rayleigh [20] and Zeleny [21] have shown that a charged drop cannot maintain its integrity for increasingly high charges; the minimum radius for which a drop maintains its integrity is called the Rayleigh limit. A detailed discussion of the calculation of the Rayleigh radius is presented in [10]. In this study, if the Rayleigh limit is reached during a calculation, it is first reached at either one of the cluster boundaries because the drop size decreases faster at those locations. In the present model the drops are described up to the Rayleigh limit; further drop splitting, although beneficial because it provides secondary atomization, is not modeled. If the Rayleigh limit is reached by drops at the inner boundary of the cluster, the computation is stopped because the model does not describe the complex and unknown splitting process, and the drops located at larger radial coordinates would be affected by such important changes. In contrast, if the Rayleigh limit is reached at the outer cluster boundary, the calculation is pursued and output of drops having reached the Rayleigh limit is further ignored because it does not affect electrostatically the behavior of drops located at smaller radial coordinates. It is also assumed that because of the small drop size after splitting, their dynamic and thermodynamic effects on the gas are negligible.

2.6 Relation between drop radius and charge

Pfeifer and Hendricks [22] studied the charge-to-mass relationship for electrohydrodynamically sprayed liquid drops and showed that it is proportional to the drop radius; however, the quantity of drop electrostatic charge may vary according to the method used for charging. In agreement

with [22], Kelly [14] showed empirically that the maximum charge sustained by a drop is

$$| q_d |_{\max} = 7.36 \times 10^{-11} R_d^0 \text{ coul.} \tag{15}$$

In the present calculations, q_{dj} is chosen to be a fraction of the maximum charge calculated from Eq. 15; there is currently no data suggesting a different dependence upon R_d^0 than that of Eq. 15.

3 Results

In order to understand the separate contributions of electrostatic dispersion which affects the drops radial motion, and that of gas and drop tangential irrotational motion and tangential solid body rotation, results were obtained for different initial conditions as shown in Table 2. In particular, it is desirable to know whether mechanical means can be used to accomplish the same degree of dispersion as the electrostatic charging, and whether mechanical means can additionally be used to substantially enhance electrostatic dispersion. The results are speculative by nature since experiments to confirm our predictions are not available; however, we expect that since the predictions from both the cluster-in-vortex model [15] and the electrostatic model [10] are in qualitative agreement with observations, the combined model maintains the same predictive qualities.

The results discussed below are all from calculations performed with an initial binary drop size distribution (R_1^0 = 2.0 x 10^{-3} cm, R_2^0 = 2.5 x 10^{-3} cm) with $\Phi^0 = 0.314$, $T_{g\infty}^0 = 600$ K, $T_{ds}^0 =$ 300 K, $Y_{F\infty}^0$ = 0.0, p = 1 atm, $R_c^0 = 2$ cm, $\hat{u}_{dr}^0 = 0.0$ cm/s, with $\max_{r_2^0}(n_2^0)/\max_{r_1^0}(n_1^0) = 1/3$. Because of the different ρ_l and molecular weights of the compounds, for identical Φ^0 and ratio $\max_{r_2^0}(n_2^0)/\max_{r_1^0}(n_1^0)$, the value of no is different for each compound. We investigate here the influence of the initial tangential velocities, of the percent of maximum drop charge and of the fuel

properties.

Figure 2 illustrates velocity results for initial-size-class-1 drops from run 1 in Table 2. Without electrostatic charge, the radial and tangential velocities are typical of a swirling flow and the drop velocity angle, calculated as the angle between the velocity vector and the tangential coordinate, is larger in the inner or central region of the cluster than at either one of its boundaries. Drop dispersion is larger for initially larger drops because of the larger centrifugal force (see Fig. 3), and there is a region of large fuel vapor partial density in the central part of the cluster (also Fig. 3) due to the larger drop number density at those locations (not shown here; see [15] and [10]).

The results presented below address the following questions: (1) Could mechanical dispersion induced by imparting a larger drop velocity *be superior to* electrostatically-induced drop dispersion for the purpose of reducing the fuel partial density? This is addressed in Section 3.1. (2) Could mechanical centrifugation be *compounded* with electrostatic dispersion to further lower the reduced partial fuel density obtained with electrostatic dispersion alone? Is it better to use gas induced centrifugation (Section 3.2) to promote both the drops motion and that of the gaseous evaporated species, or is it better to use drop induced centrifugation to move the drops to increased radial locations where they will deposit the evaporated fuel (Section 3.3)? (3) How do these effects depend upon fuel properties (Section 3.4)?

3.1 Drop induced mechanical centrifugation versus electrostatic dispersion

Drop charging results in a dramatic increase in the radial velocities and in a reduction of nonuniformities of the dependent variables as the cluster expands much faster and the drop number densities

for each initial-size class decrease; the consequence of these changes is to reduce the mass fraction of the evaporated compound and thus the propensit y to form soot. The difference between drop-induced dispersion and elect rest at ic dispersion is best understood by examining in runs 1 and 12 plots of the velocity angle, θ, where tan $\theta = |u_{dr}| / |u_{d\theta}|$ in Fig. 4. For uncharged drops, $\theta < 45^o$ and thus $|u_{dr}| < |u_{d\theta}|$. For charged drops, $\theta < 45°$ in the inner part of the cluster and $\theta > 45°$ in the outer part of the cluster; thus $|u_{dr}| < |u_{d\theta}|$ in the inner part of the cluster and $|u_{dr}| > |u_{d\theta}|$ in the outer part of the cluster. Therefore, dispersion is controlled by $u_{d\theta}$ for uncharged clusters, whereas dispersion is controlled by $u_{d\theta}$ in the inner part of cluster and by u_{dr} in the outer part of the cluster for charged clusters. Because it is $B^0_{d\theta}$ which affects $u_{d\theta}$ at larger r locations, runs 1-3 represent the most judicious way of mechanically enhancing dispersion in the outer portion of the cluster by increasing $u_{d\theta}$.

Drop evaporation depends mainly upon T_{gi}, $\overrightarrow{u}_{sj}$ and Y_{Fi}, all of which depend upon drop dispersion. As the drops disperse, the cluster engulfs hot, unvitiated air from the surroundings and this promotes evaporation. In contrast, $\overrightarrow{u}_{sj}$ decreases with increasing time, and this hinders evaporation. For uncharged clusters of drops, the relaxation of $\overrightarrow{u}_{sj}$ continues throughout the drop lifetime, irrespective of the position within the cluster; for charged clusters of drops, a finite value of $\overrightarrow{u}_{sj}$ is maintained in the outer portion of the cluster by the continuous contribution of the electrostatic force (which is an increasing function of r) to u&. In this manner, electrostatic charging compounds the advantage of dispersion to evaporation.

3.1.1 Effect of $A^0_{d\theta}$

Comparisons of results obtained in runs 4 and 5 show that for the very large irrotational motion chosen in these calculations, the drop number density increases substantially towards the inner

cluster boundary and a front of drops is created which travels towards the outer boundary (not illustrated). In absence of charging, the drop number density is larger towards the inner cluster boundary and smaller toward the outer cluster boundary as the drop dispersion does not benefit of the added effect of the electrostatic charging. This produces a somewhat denser cluster, a lower temperature (due to the larger amount of heat transferred to the drops) and larger Y_{Fi} (due to the compounded effect of the larger number of drops) towards the inner boundary (Fig. 4), and the opposite towards the outer cluster boundary. Significantly, for uncharged drops, the larger ρ_{gi} at the locations of the lower temperature corresponds also to the location of the larger Y_{Fi} thus also increasing the value Of $Y_{Fi}\rho_{gi}$ (Fig. 4); an increase in this value is an indication of more intense nucleation, producing a larger amount of soot precursors.

Since increases in $A^0_{d\theta}$ result in the formation of denser regions in the cluster thereby enhancing soot nucleation, no further calculations were performed with uncharged drops and larger values of $A^0_{d\theta}$ (trying to achieve mechanical dispersion equivalent to the charged drop dispersion) because it is obviously an unsuccessful approach.

3.1.2 Effect of $B^0_{d\theta}$

Results from runs 1-3 were compared with those from run 12 to first determine the difference introduced by the electrostatic charge at otherwise identical conditions (runs 1 and 12), and second to explore the possibility of achieving dispersion similar to that induced by electrostatic forces by increasing the initial drop tangential solid body rotation (runs 2, 3 and 12).

Examination of the angle of the drop velocity vector with the tangential direction (Fig. 5) reveals that the maximum drop velocity angle for uncharged clusters of drops is near the cluster inner boundary and is almost insensitive to $B^0_{d\theta}$ (ranges from 33° to 35° for initial-size-class-1),

whereas the maximum velocity angle for charged clusters of drops is near the outer boundary (68o for initial-size-class-1). This is because the maximum near the inner boundary is due to the acquired irrotational motion of the drops resulting from momentum transfer with the gas which is similar in runs 1-3, whereas the maximum near the outer boundary is due to the electrostatic force enlarging the radial component of the drop velocity. Additionally, the ranges of maximum velocity angles for the two initial-size classes show that when charging the drops according to Eq. 15, it is the smallest initial-size class that is preferentially dispersed, whereas in the absence of charge it is the largest initial-size class which is preferentially dispersed. Since smaller drops heat up faster, and thus evaporate faster, this preferential centrifugation promotes mixing and thus provides an additional benefit from electrostatic charging.

Increasing $B_{d\theta}^0$ results in increasing expansion, faster engulfment of hot gas by the cluster and thus faster evaporation. However, when the drops are uncharged, even for $B_{d\theta}^0$ = 450 S-land the same cluster expansion (of 3.75 cm), the values of Y_{Fi} and ρ_{gi} are larger than when the drops are electrostatically charged and $B_{d\theta}^0$ = 200 s^{-1}. It is not only the maximum values that differ in the uncharged versus the charged situation but also the profiles: the maximum Y_{Fi} occurs in the first case near the outer boundary and in the second case it appears as a plateau in the central part of the cluster (Fig. 6). For uncharged drops, the maximum ρ_{gi} moves with increasing $B_{d\theta}^0$ from being near the outer boundary to being near the inner boundary (Fig. 7); it is also near the inner cluster boundary in the charged drops case. The Y_{Fi} profile is determined by the drops motion and evaporation whereas the ρ_{gi} profile is determined by T_{gi}. Since nucleation of soot precursors depends upon $Y_{Fi}\rho_{gi}$, the fact that for low $B_{d\theta}^0$ the maxima of Y_{Fi} and ρ_{gi} occur at the same approximate location enhances the potential for soot nucleation.

3.2 **Gas dispersion for charged drops**

3.2.1 Effect of $A^0_{g\theta}$

The value of $A^0_{g\theta}$ *was* decreased by a factor of 2 to 100 from run 6 to run 12 to investigate the influence of gas tangential irrotational motion upon gaseous species (evolved from the charged drops) dispersion. The larger gas irrotational motion is transferred to the drops and this induces a larger centrifugation at the inner cluster boundary creating a large moving front of drops at that location. Since the effect of the irrotational motion decreases as r^{-1}, the central and outer portion of the cluster do not benefit as much from the increased $A^0_{g\theta}$; in particular, initial-size- class-2 is more affected by the larger $A^0_{g\theta}$ since it is less centrifuged by the electrostatic force. 'I'he result of a larger $A^0_{g\theta}$ is an increase in the velocity angle at the inner boundary (not shown), and an increase in the nonuniformities of the drop number densities and residual radii (not shown). Comparisons between the Y_{Fi} and ρ_{gi} profiles for the two cases show that they are very similar except for somewhat lower values toward the inner cluster boundary (not shown).

Thus, within the range studied here, the gas tangential irrotational motion does not provide substantial additional benefits. However, since electrostatic charging promotes the dispersion of the smaller drops, the gas irrotational motion might have the important role of enhancing the centrifugation of the larger, and thus more difficult to heat drops, and promoting their contact with the hotter surrounding gas.

3.2.2 Effect of $B^0_{g\theta}$

The effect of the gas tangential solid body rotation has been studied by comparing results from several calculations: (1) runs 9-11 ($B^0_{g\theta}$ = 100 s-1, *200* s^{-1}, and 300s-^{1} respectively) with $A^0_{g\theta}$ = 100

cm^2/s and $B^0_{d\theta}$ = 200 s^{-1}, and (2) runs 6 and 8 ($B^0_{g\theta}$ = O $s^{-1}$and 100 s^{-1}) with $A^0_{g\theta}$ = *200* cm^2/s and $B^0_{d\theta}$ = 200 s^{-1}.

The gas tangential solid body rotation is transmitted to the drops through momentum coupling and promotes the drops tangential motion. Since the solid body rotation becomes more important with increasing distance from the vortex center, it is only the outer part of the cluster that might be affected. Inspection of the results shows that the effect of $B^0_{g\theta}$ *is* negligible within the range studied. This is because on the one hand the larger drop tangential velocity results in a smaller velocity angle away from the inner cluster boundary thus tending to hinder dispersion, engulfment of hot surrounding gas and evaporation; on the other hand, the larger drop tangential velocity at larger locations promotes drop heating and evaporation. The two effects balance for the range of $B^0_{g\theta}$ studied here and the values of Y_{Fi} and ρ_{gi} are very similar (not shown).

With increasing $B^0_{g\theta}$, it is expected that it is predominantly the smaller initial-size class which will be affected. If dispersion of these faster heating drops is hindered, this will somewhat counteract the beneficial electrostatic charge effect; if dispersion of these drops is enhanced, this will induce a spatial segregation by initial-size class whose effects on soot nucleation are difficult to assess a priori.

3.3 Drop induced mechanical dispersion of charged drops

3.3.1 Effect of $A^0_{d\theta}$

As discussed above, a large $A^0_{d\theta}$ creates towards the inner cluster boundary a front of traveling drops, increases the drop number density and accordingly aggravates nucleation processes. Comparisons bet ween results obtained with runs 5 and 12 (Fig. 8) show that for charged clusters of drops, the

beneficial effect of charging is substantially decreased by increasing $A^0_{d\theta}$ from O to 200 cm^2/s. At locations c1osc to the inner cluster boundary, the large irrotational motion dominates the small electrostatic force and very large nonuniformities are created with larger than initial n (Fig. 8) resulting in smaller T_{gi}, larger Y_{Fi} (Fig. 8) and larger ρ_{gi} (Fig. 8) than when $A^0_{d\theta}$ is null. At locations close to the outer cluster boundary, the irrotational motion is smaller and the electrostatic force dominates the drop's dispersion resulting in smaller departures from the situation when $A^0_{d\theta} = O$ cm^2/s. The difference in dispersion between the two cases is best illustrated by the velocity angle: for null $A^0_{d\theta}$, the angle is <45° towards the inner cluster boundary whereas it is >50° towards the outer boundary and remains larger during the entire calculation for larger r; for finite $A^0_{d\theta}$, the angle becomes >45° in the entire cluster and eventually decays to <45° towards the end of the calculation. When $A^0_{d\theta}$ = 200 cm^2/s, parts of the cluster adjacent to the inner boundary remain in a dense configuration during the entire drop lifetime, thus defeating the purpose of the electrostatic charging.

3.3.2 Effect of $B^0_{d\theta}$

Results from runs 7 and 12 were compared to investigate the effect of $B^0_{d\theta}$ on charged drops. Increasing $B^0_{d\theta}$ by 50% produced slightly increased' cluster expansion. Due to the compounded effect of the larger solid body rot at ion and the electrostatic force, the velocity angle is (>45° and) smaller everywhere except at the inner cluster boundary (where it is similar) showing that as expected, u_{dr} is relatively smaller than $u_{d\theta}$. Both Y_{Fi} and ρ_{gi} have similar values in both calculations (Fig. 9) except at locations near the outer cluster boundary where they are slightly larger with increasing $B^0_{d\theta}$ due to the lower T_{gi} resulting from the larger n. The larger n (Fig. 9) is a direct consequence of the larger $B^0_{d\theta}$ at that location. Thus, it is interesting to notice that the benefits associated with

electrostatic charging (in terms of potential soot nucleation) seem to decrease as $B_{d\theta}^{0}$ is increased.

3.4 **Effect of fuel properties**

Since without drop charge the most promising mechanical means of enhancing dispersion is through increasing $B_{d\theta}^{0}$, its effects are compared to those of electrostatic charging for all three fuels. Similarly to the results obtained with BV, for both QUAD and DHBV drop charging is considerably superior to increased mechanical dispersion within the range of $B_{d\theta}^{0}$ studied here (Figs. 1011, and Figs. 12-13). Thus, it is proposed that the general benefit of electrostatically induced versus mechanical (in the range studied) dispersion is independent of fuel properties.

Fuel specificity is compared in Fig. 14 where Y_{Fi} and ρ_{gi} are plotted at the same physical time for all three fuels for runs 1, 3, 12, and 13-18; it is important to remember that Φ^{0} is identical in all runs, but no is different (the drop count is: 6.81223 x 10^{5} for BV; 8.20483x 10^{5} for DHBV; 8.82291 x 10^{5} for QUAD) because its value is related to both ρ_{l} and w. For uncharged drops and low $B_{d\theta}^{0}$ both Y_{Fi} and ρ_{gi} for BV are somewhat similar to QUAD and much lower than for DHBV; this is despite the fact that QUAD and DHBV have similar n^{0}. Thus, in the absence of charge it is the latent heat that determines soot propensity, irrespective of n^{0}. This is a novel result since the accepted assumption [9] is that soot propensity for liquid sprays depends mostly of n^{0} and its dependence on fuel properties versus operating conditions has not been documented. When $B_{d\theta}^{0}$ is increased, the effect of no becomes important and now there is an additional difference between Y_{Fi} for BV and QUAD, with the soot propensity being lower for BV. Since at otherwise identical initial conditions no is predominantly determined by ρ_{l}, the conclusion is that p_{l} becomes increasingly important with increasing $B_{d\theta}^{0}$. This result is consistent with the previous interpretation [10] of soot propensity being

the result of two competing characteristic times: the evaporation time and the dispersion time. Here the evaporation time is governed by the latent heat and the dispersion time by the liquid density.

When the drops are charged but $B^0_{d\theta}$ is small, the results are reminiscent of the situation for uncharged drops. Thus, charging does not change the effect of fuel properties upon soot propensity.

4 Summary and Conclusions

The effect of mechanical dispersion on uncharged and electrostatically charged polydisperse clusters of drops has been numerically investigated. The cluster of drops is embedded into a cylindrical axisymmetric vortex that moves through a region of increasing temperature. The drops are centrifuged by the vortex and the cluster forms an inner and outer cylindrical boundary. At the inner boundary, the cluster is in contact with a gaseous vertical region devoid of drops while at the outer boundary, the cluster is in contact with a hot gas (air) that it engulfs as the drops are centrifuged by the vortex. The model has been exercised for an initially binary size distribution by varying the drops charge and the initial gas and drop tangential motion.

It has been shown that dropinduced mechanical centrifugation cannot achieve the same beneficial effects as electrostatic dispersion in terms of decreasing both the mass fraction of the evaporated compound and the gas density to reduce soot nucleation while promoting evaporation. This is because increasing the drops tangential irrotational motion increases the drop number density near the inner cluster boundary and this promotes soot nucleation. Increasing the drops tangential solid body rotation disperses the cluster at locations further from its inner boundary; however, the slip velocity between drops and gas cannot be maintained, as it is for charged drops, and its added enhancement to evaporation is lost. Thus, electrostatic charging is superior to mechanical

centrifugation for combined soot nucleation reduction and enhancement of evaporation,

Since mechanical dispersion cannot compete with electrostatic dispersion, the idea of combining them to promote greater reduction of the partial mass fraction of the evaporated compound has been investigated as well. Both gas-induced and drop-induced centrifugation were explored for charged clusters of drops.

Within the range of values investigated, gas-induced dispersion by irrotational motion does not provide substantial additional dispersion for charged drops; thus it does not contribute substantially to soot propensity reduction. However, since the electrostatic charge is proportional to the initial drop radius and thus it disperses preferentially the smaller initial-size class, whereas the irrotational motion is most effective at smaller radial locations and thus affects the larger initial-size class (which is less affected by the electrostatic force), the added effect of the gas tangential irrotational motion is to promote centrifugation of the larger drops through momentum transfer, and thus to enhance evaporation. A larger gas tangential solid body rotation has been seen to be ineffective to reduce soot propensity within the range of values studied. This is because although the larger drop tangential velocity results in a smaller velocity angle away from the inner cluster boundary (tending to hinder dispersion, engulfment of hot surrounding gas and evaporation), it also promotes drop heating and evaporation. The two effects balance with no noticeable effect on the partial density of the evaporated compound.

Drop-induced dispersion by irrotational motion has been shown to promote soot nucleation through the formation of a region of very large drop number density near the inner cluster boundary. Increasing the drops tangential solid body rotation did not affect central or near the inner boundary cluster regions, but it increased the drop number density at the outer cluster boundary thereby promoting soot nucleation.

Thus, mechanical dispersion can neither compete with electrostatic dispersion to reduce soot nucleation, nor benefits noticeably soot nucleation reduction when added to electrostatic dispersion.

Our results indicate that, generally, drop dispersion hinders the initiation of nucleation reactions, and thus can be considered to impede soot formation; once soot is formed, increased dispersion might also promote soot oxidation (and thus soot reduction), however, this aspect has not been investigated in this study. The manner in which drop dispersion is produced has also an effect on soot propensity; for example, imparting solid body rotation has been found to be favorable to soot reduction, whereas imparting irrotational motion has been found to promote soot formation in some regions.

The effect of fuel properties has also been studied and it was shown that for uncharged drops it is the latent heat that dominates soot propensity at small drop dispersion, whereas the liquid density becomes increasingly important with increasing drop dispersion. Drop charging does not affect the effect of fuel properties upon soot propensity.

In absence of documented data for comparison with the model predictions, the above results are somewhat speculative until confirmed by experimental observations.

ACKNOWLEDGMENT

This research was conducted at the Jet Propulsion Laboratory, California Institute of Technology under the sponsorship of the Office of Naval Research with Dr. Gabriel Roy as contract monitor under an agreement with the National Aeronautics and Space Administration.

References

[1] Glassman, I., Soot Formation in Combustion Processes, 22nd *Symp.(Int.)* on *Combustion*, pp. 295-311, 1988.

[2] Kadota, T., Hiroyasu, H., and Farazandehmer, A., Soot Formation by Combustion of a Fuel Droplet in High Pressure Gaseous Environments, *Combust. Flame*, vol. 29, pp. 67-75, 1977.

[3] Nakanishi, K., Kadota, T. and Hiroyasu, H., Effect of Air Velocity and Temperature on the Soot Formation by Combustion of a Fuel Droplet, *Combust. Flame*, vol. 40, pp. 247-262, 1981.

[4] Kadota, T., and Hiroyasu, H., Soot Concentration Measurement in a Fuel Droplet Flame via Laser Light Scattering, *Combust. Flame*, vol.55, pp. 195-201, 1984.

[5] Randolph, A. L. and Law, C. K., Time Resolved Gasification and Sooting Characteristics of Droplets of Alcohol/Oil Blends and Water/Oil Emulsions, *21st Symp.(Int.) on Combustion*, pp. *1125-1131, 1986.*

[6] Lee, K-O., Jensen, K. A. and Choi, M. Y., Investigation of Sooting in Normal-Gravity Droplet Combustion Using Light Extinction and Gravimetric Techniques, *26th Symp.(Int.) on Combustion*, pp. 2397-2404, 1996.

[7] Law, C. K., Combustion Studies of Energetic Liquid Materials, *Proceedings of the 7th ONR Propulsion Meeting*, p.1 10-116, 1994.

[8] Kadota, T., Henien, N. A. and Lee, D. U., Time Resolved Soot Particulate in Autoignited Intermittent Spray Flames, *18th Symp.(Int.) on Combustion*, pp. 329-336, 1981.

[9] Sangiovanni, J. J. and Liscinsky, D. S., Soot Formation Characteristics of Well-Defined Spray Flames, *20th Symp. (Int.) on Combustion*, pp. 1063-1073, 1984.

[10] Bellan, J. and Harstad, K., Electrostatic Dispersion and Evaporation of Clusters of Drops of High-Energy Fuel for Soot Control, *26th Symp. (Int.) on Combustion*, pp. 1713-1722, 1996.

[11] Bellan, J., Electrostatic Dispersion and Evaporation of Dense and Dilute Clusters of Drops of High-Energy Fuel for Soot Control, *Proceedings of the 8th ONR Propulsion Meeting*, p. 168-182, 1995.

[12] Santoro, R. J., private communication, 12/1/1995.

[13] Bellan, J. and Harstad, K., Ignition of a Binary-Fuel (Solvent-Solute) Cluster of Drops, *Comb. Sci. and Techn.*, vol. 119, pp. 331-373, 1996.

[14] Kelly, A. J., The Electrostatic Atomization of Hydrocarbons, *J. of Inst. of Energy*, vol. 51, no. 431, pp. 312-320, 1984.

[15] Harstad, K. and Bellan, J., Behavior of a Polydisperse Cluster of Drops Evaporating in an Inviscid Vortex, *Int. J. Multiphase Flow*, vol. 23, no. 5, 899-925, 1997.

[16] Bellan, J. and Cuffel, R., A Theory of Non Dilute Spray Evaporation Based upon Multiple Drop Interactions, *Combust. and Flame*, vol. 51, pp. 55-67, 1983.

[17] Bellan, J. and Harstad, K., Turbulence Effects During the Evaporation of Drops in Clusters, *Int. J. Heat Mass Transfer*, vol. 31, no. 8, pp. 1655-1668, 1988.

[18] Bellan, J. and Harstad, K., The Details of the Convective Evaporation of Dense and Dilute Clusters of Drops, *Int. J. Heat Mass Transfer*, vol. *30*, no. *6*, pp. 1003-1093, 1987.

[19] Cliffe, K. A. and Lever, D. A., Isothermal Flow Past a Blowing Sphere, *Int. J. Numer. Meth. Fluids,* vol. 5, *pp. 709-725, 1985.*

[20] Rayleigh, Lord, On the Equilibrium of Liquid Conducting Masses Charged with Electricity, *Phil. Mug.*, vol. 14, pp. 184-186, 1882.

[21] Zeleny, J., On the Conditions of Instability of Electrified Drops with Applications to the Electrical Discharge from Liquid Points, *Proc. Cambridge Phil. Soc.*, vol. *18, pp. 71-83, 1916.*

[22] Pfeifer, R. J. and Hendrick, C. D., Charge-to-Mass Relationship for Electrohydrodynamically Sprayed Liquid Droplets, *The Phys.* Fluids, vol. 10, no. 10, pp. 2149-2154,1967.

Symbol	Benzvalene	Quadricyclane	Dihydrobenzvalene
$\Phi_s \equiv$ air mass/fuel mass	13.2	13.4	13.7
w, g/mole	78.12	92.14	80.14
T_{bn}, K	353	382	344
L_{bn}, cal/g	96.90	96.85	74.50
ΔC_p, cal/(gK)	6.8×10^{-2}	1.48×10^{-3}	0 (assumed)
ρ_l, g/cm^3	0.879	0.7	0.71
C_{pl}, cal/(gK)	0.415	0.36	0.432
μ_l, g/(ems)	0.392 x10-2	0.316 x10-2	0.35x 10^{-2} (assumed)
$D_{ml}(Le_l = 10)$, cm^2/s	0.995×10^{-4}	0.999×10^{-4}	0.978×10^{-4}
λ_l, cal/(gK)	3.63x 10^{-4}	2.67x 10-4	3×10^{-4}
$C_{pg}(T_g = \sqrt{300 \times 600})$	0.37	0.435	0.437

Table 1: Properties of high-energy fuels

Run #	% $\lvert q_d \rvert_{max}$	$A^0_{d\theta}$, cm^2/s	$B^0_{d\theta}$, s-1	$A^0_{q\theta}$, cm^2/s	$B^0_{q\theta}$, S--l	Fuel
1	0	0	200	100	0	BV
2	0	0	350	100	0	BV
3	0	0	450	100	0	BV
4	0	200	200	100	0	BV
5	0.25	200	200	100	0	BV
6	0.25	0	200	200	0	BV
7	0.25	0	300	100	0	BV
8	0.25	0	200	200	100	BV
9	0.25	0	200	100	100	BV
10	0.25	0	200	100	200	BV
11	0.25	0	200	100	300	BV
12	0.25	0	200	100	0	BV
13	0	0	200	100	0	DHBV
14	0	0	450	100	0	DHBV
15	0.25	0	200,	100	0	DHBV
16	0	0	200	100	0	QUAD
17	0	0	450	100	0	QUAD
18	0.25	0	200	100	0	QUAD

Table 2: Percent of maximum charge anti initial tangential velocities.

FIGURE CAPTIONS

Figure 1. Physical configuration of the cluster-in-vortex for a binary size distribution.

Figure 2. Radial drop velocity (a), tangential drop velocity (b), and drop velocity angle (c) profiles for initial-size-class-1 for run 1. Symbols correspond to the following times: $.4x $10^{-5}s$ (+); 9.2 x10^{-4}s (0); 2.6 x10^{-3}s (△); 5.9 x10^{-3}s (▽); 1.2 x10^{-2}s (0); 2.5 x10^{-2}s (◯).

Figure 3. Residual drop radius for initial-size-class-1 (a) and initial-size-class-2 (b), fuel mass fraction (c) and gas density (d) for run 1. Symbols correspond to the same times as in Fig. 2.

Figure 4. Effect of the drop charge compared to that of the initial irrotational component of the drop tangential velocity: Fuel mass fraction and gas density profiles for runs 1 (a), 4 (b) and 5 (c). Symbols correspond to the following times: 8.4x 10^{-5}s (+); 9.2x 10^{-4}s (o); 1.8x 10^{-3}s (A); 2.6 x10^{-3}s (v); 5.9 x10^{-3}s (0); 7.6 x10^{-3}s (◯).

Figure 5. Effect of the drop charge compared to that of the initial solid body rotation component of the tangential drop velocity: Velocity angle for initial-size-class-l for runs 1 (a); 2 (b); 3 (c); and 12 (d). Symbols correspond to the following times: 8.4x 10^{-5}s (+); 9.2x 10^{-4}s (o); 1.8x 10^{-3}s (△); 2.6 x10^{-3}s (v); 5.9x 10^{-3}s (0); 1.2x $10^{-2}s$ (◯); 1.6 x10^{-2}s (D)

Figure 6. Effect of the drop charge compared to that of the initial solid body rotation component of the tangential drop velocity: Fuel mass fraction for runs 1 (a); 2 (b); 3 (c); and 12 (d). Symbols correspond to the same times as in Fig. 5.

Figure 7. Effect of the drop charge compared to that of the initial solid body rotation component of the tangential drop velocity: Gas density for runs 1 (a); 2 (b); 3 (c); and 12 (d). Symbols correspond to the same times as in Fig. 5.

Figure 8. Effect of the initial irrotational component of the drop tangential velocity for charged drops: drop number density, fuel mass fraction' and gas density profiles for runs 12 (a) and 5 (b). Symbols correspond to the following times: 8.4 x10^{-5}s (+); 9.2 x10^{-4}s (o); 1.8x 10^{-3}s (A); 2.6x 10^{-3}s (v); 5.1 x10^{-3}s (0); 5.9 x10^{-3}s (◯); 7.6 x10^{-3}s (D); 1.2 x10^{-2}s (a); I..4x10^{-2}s (U); and 1.5 x10^{-2}s (n).

Figure 9. Effect of the initial solid body rotation component of the drop tangential velocity for charged drops: Drop number density, fuel mass fraction and gas density profiles for runs 12 (a) and 7 (b). Symbols correspond to the following times: 8.4x 10^{-5}s (+); 9.2x 10^{-4}s (0); 1.8x 10^{-3}s (A); 2.6 x10^{-3}s (v); 5.1 x10^{-3}s (□); 5.9 x10^{-3}s (◯); 7.6 x10^{-3}s (D); 1.2 x10^{-2}s (a); 1.4 x10^{-2}s (u); and 1.5 x10^{-2}s (n).

Figure 10. Effect of the drop charge compared to that of the initial solid body rotation component of the tangential drop velocity for DHBV: Drop number density and velocity angle for initial-size-class-1 for runs 13 (a), 14 (b) and 15 (c). Symbols correspond to the following times: 6.8x 10^{-5}s (+); 7.4 x1 0^{-4}s (o); 1.4 x1 0^{-3}s (△); 3.4 x1 0^{-3}s (v); 4.8 x1 0^{-3}s (□); 9.5 x1 0^{-3}s (◯).

Figure 11. Effect of the drop charge compared to that of the initial solid body rotation component of the tangential drop velocity for DHBV: Fuel mass fraction and gas density profiles for runs 13 (a), 14 (b) and 15 (c). Symbols correspond to the same times as in Fig. 10.

Figure 12. Effect of the drop charge compared to that of the initial solid body rotation component of the tangential drop velocity for QUAD: Drop number density and velocity angle for initial-size-class-1 for runs 16 (a), 17 (b) and 18 (c). Symbols correspond to the following times: 6.7x 10^{-5}s (+); 7.3 x1 0^{-4}s (o); 1.4×10^{-3}s (△); 2.1 x1 0^{-3}s (▽); 3.4 x1 0^{-3}s (□); 5.4 x1 0^{-3}s (()); 6.7 x1 0^{-3} s(D).

Figure 13. Effect of the drop charge compared to that of the initial solid body rotation component of the tangential drop velocity for QUAD: Fuel mass fraction and gas density profiles for runs 16 (a), 17 (b) and 18 (c). Symbols correspond to the same times as in Fig. 12.

Figure 14. Effect of fuel properties: Fuel mass fraction and gas density profiles for BV(+), DHBV (◇)and QUAD (△)at 3.4 x 10^{-3}s for runs 1, 13 and 16 (a); 3, 14 and 17 (b); and 12, 15 and 18 (C).

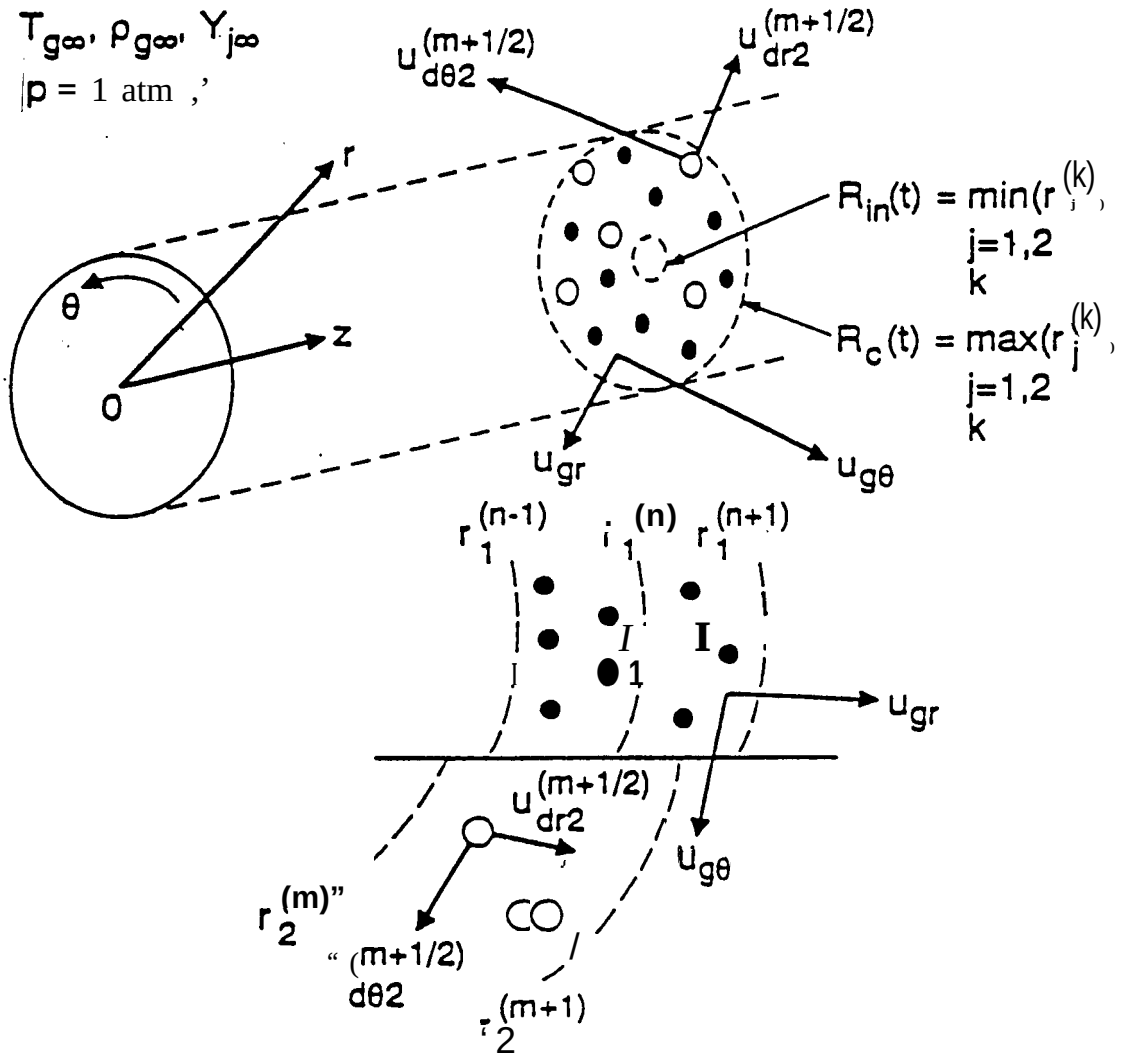
$T_{g\infty}$, $\rho_{g\infty}$, $Y_{j\infty}$
p = 1 atm
$u_{d\theta 2}^{(m+1/2)}$
$u_{dr2}^{(m+1/2)}$
r
θ
z
0
$R_{in}(t) = \min(r_j^{(k)})$, j=1,2, k
$R_c(t) = \max(r_j^{(k)})$, j=1,2, k
u_{gr}
$u_{g\theta}$
$r_1^{(n-1)}$
$r_1^{(n)}$
$r_1^{(n+1)}$
I_1
u_{gr}
$u_{dr2}^{(m+1/2)}$
$u_{g\theta}$
$r_2^{(m)}$
$u_{d\theta 2}^{(m+1/2)}$
$r_2^{(m+1)}$

Figure 1

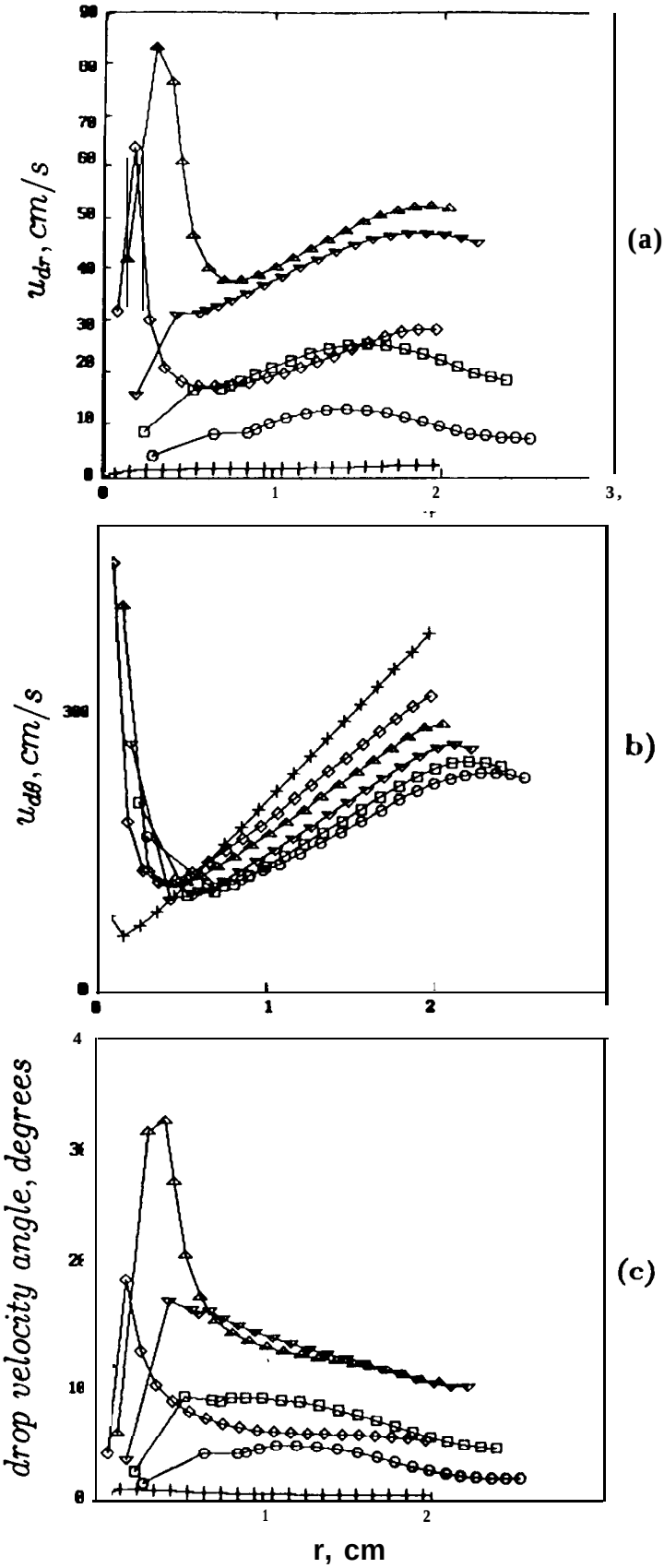

Fig 2

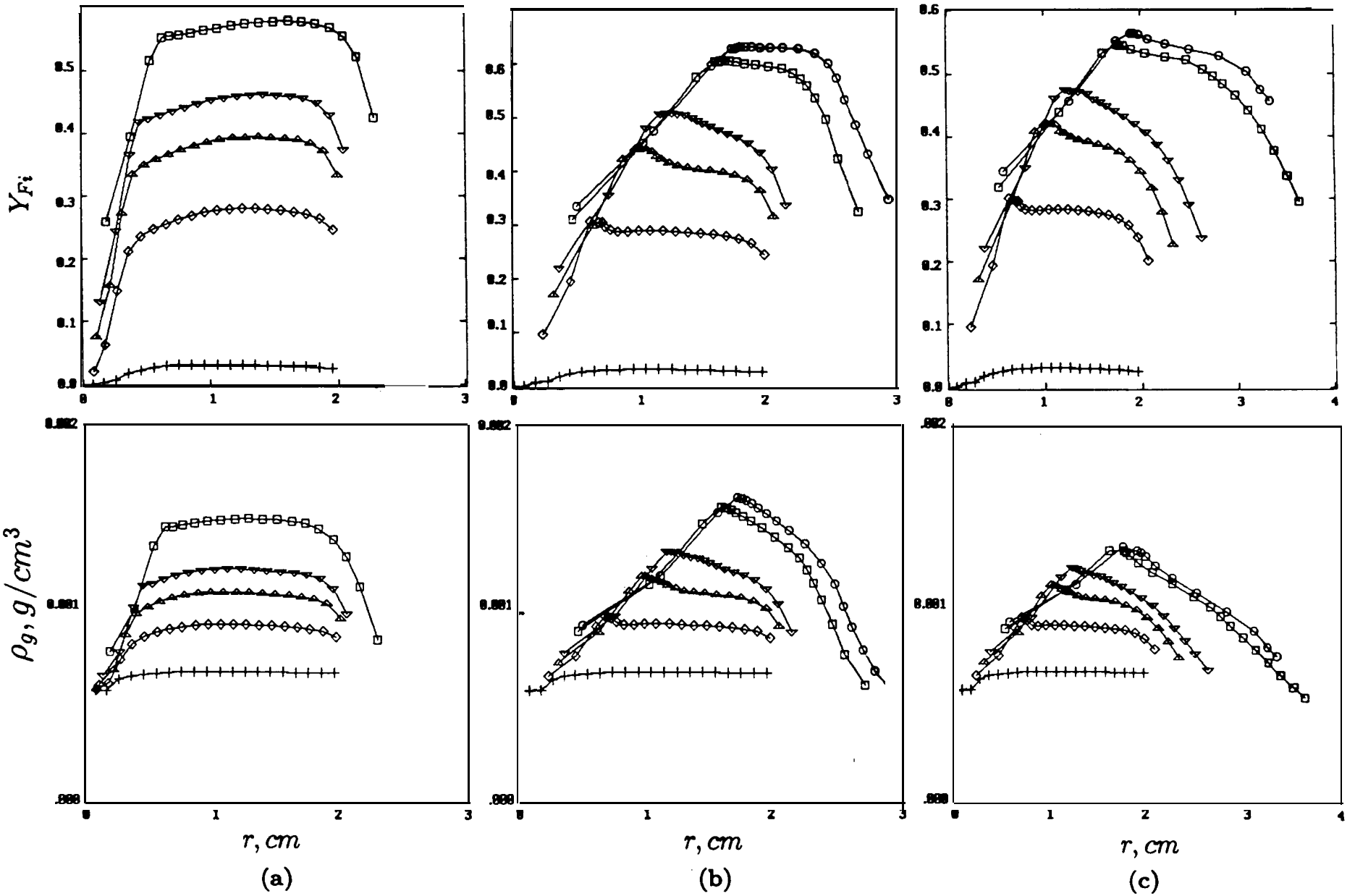
Y_{Fi}
$\rho_g, g/cm^3$
r, cm
(a)
(b)
(c)

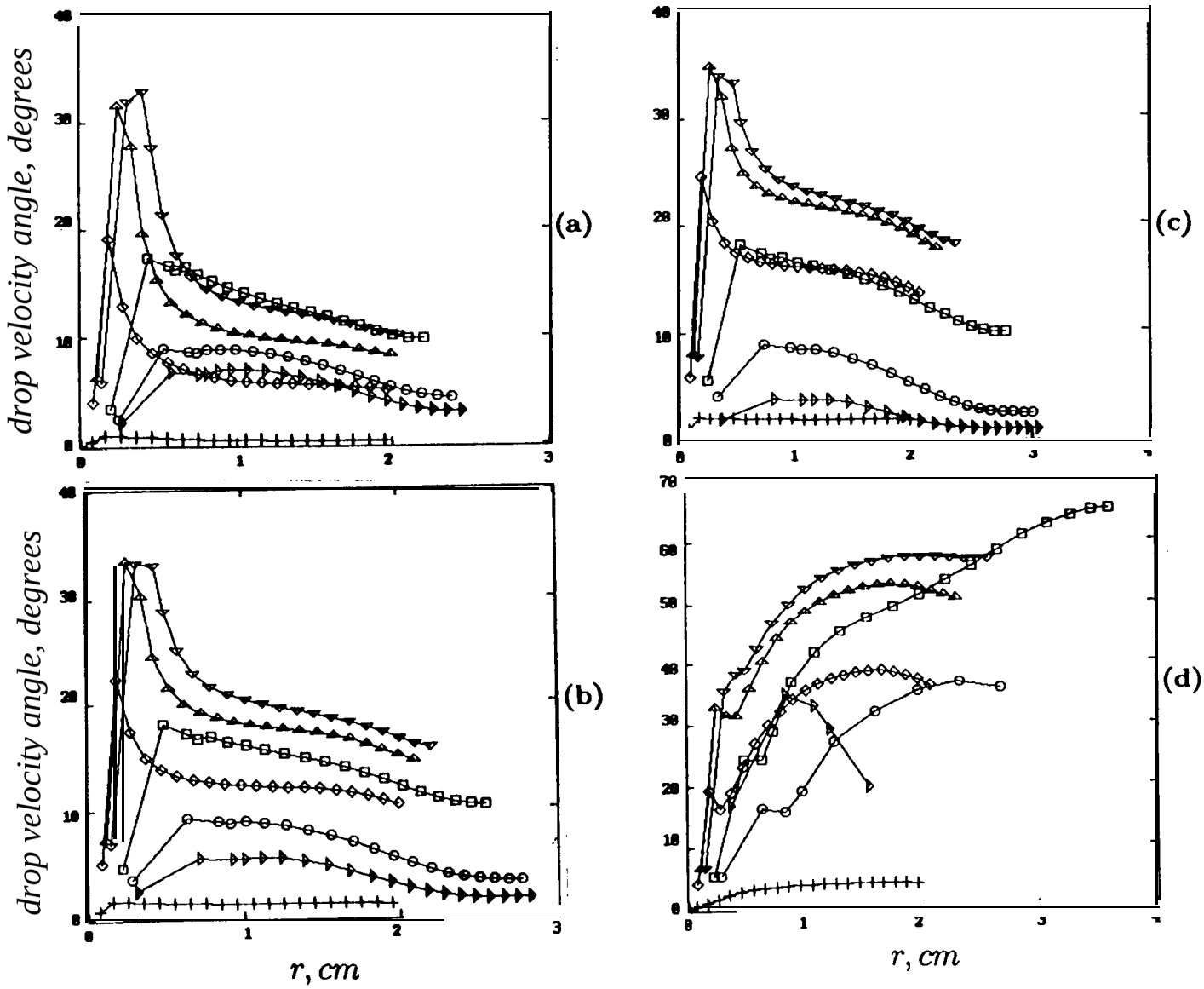

Fig 5

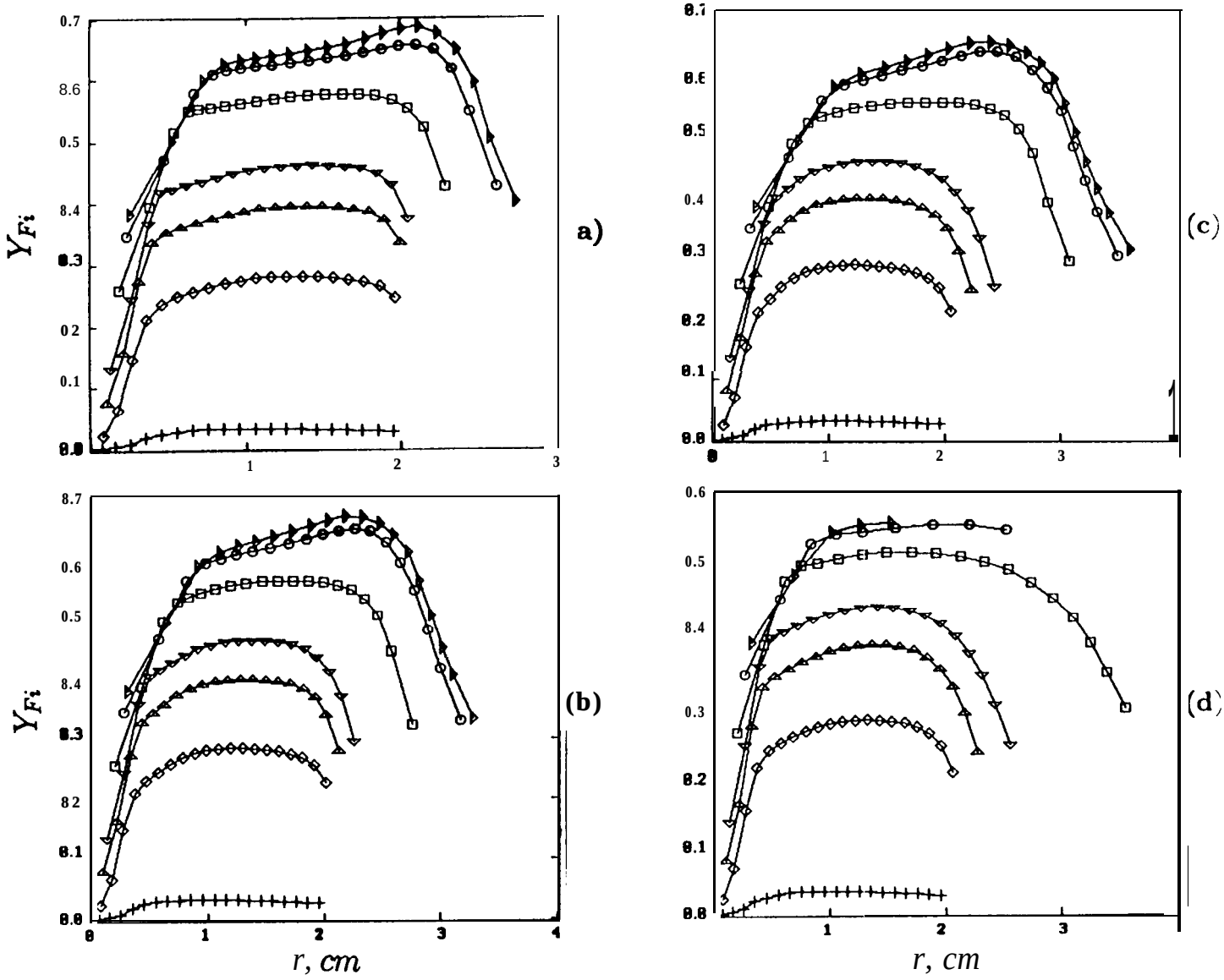

Fig 6

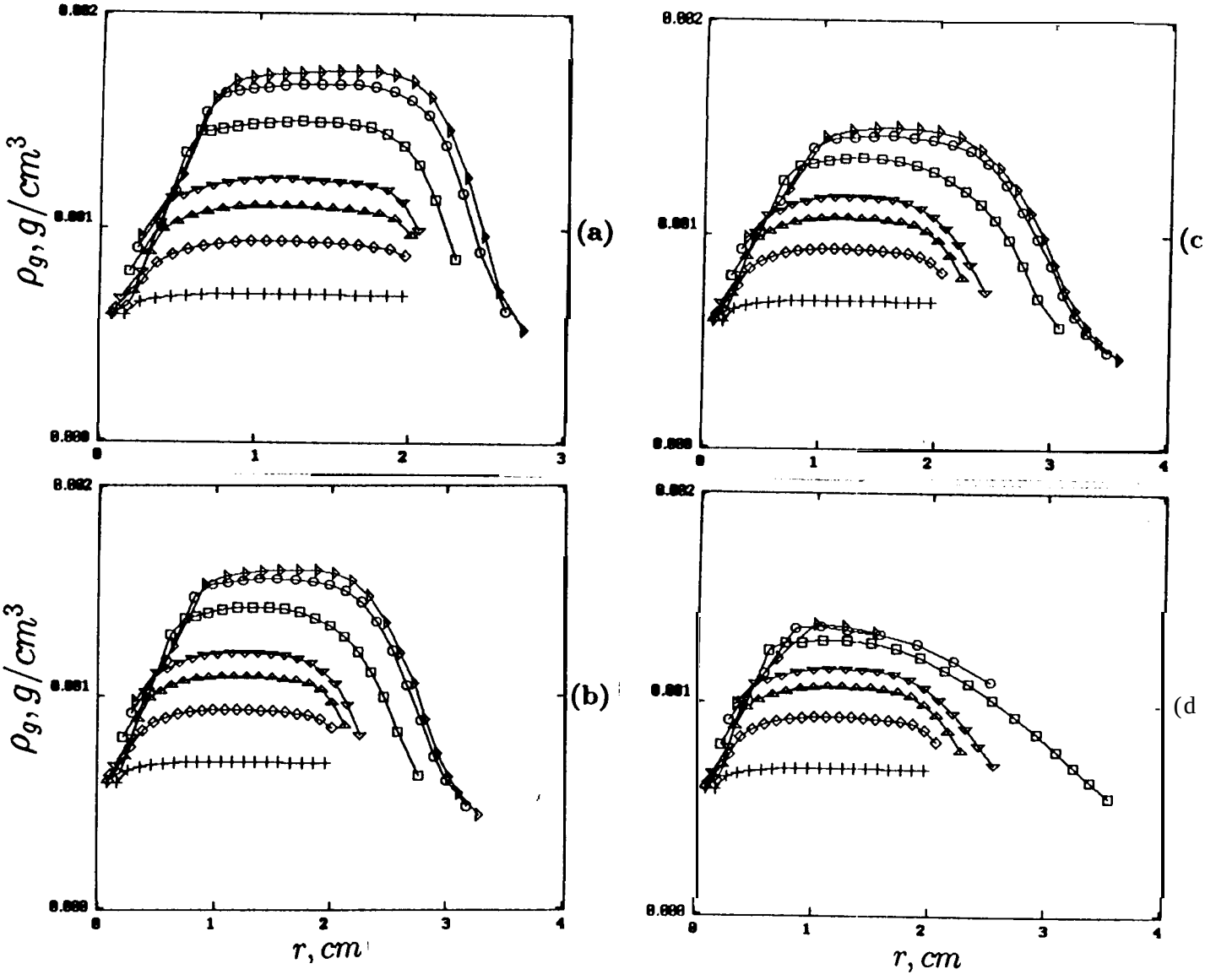

Fig 7

Fig 8

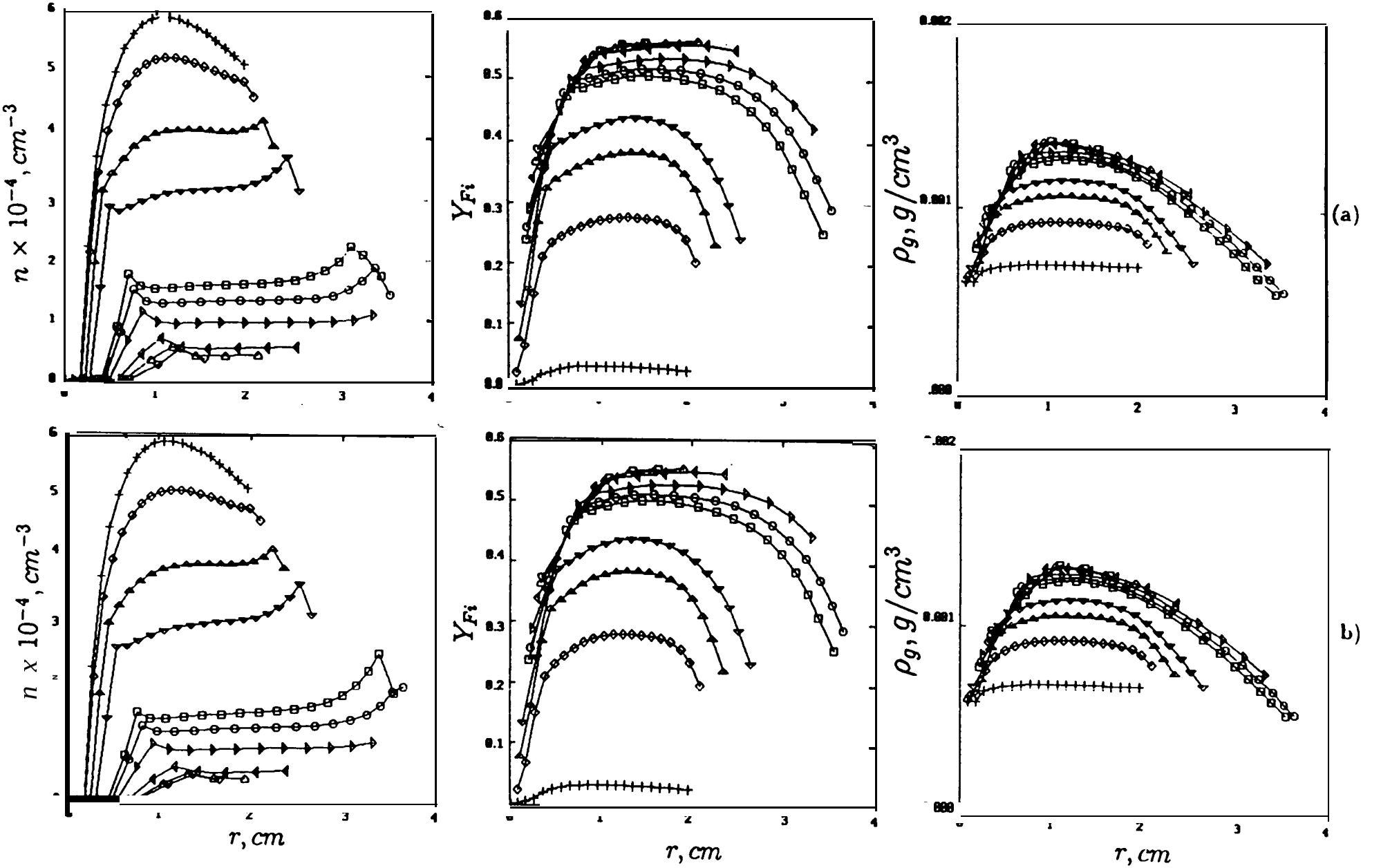
$n \times 10^{-4}, cm^{-3}$
Y_{Fi}
$\rho_g, g/cm^3$
(a)
$n \times 10^{-4}, cm^{-3}$
Y_{Fi}
$\rho_g, g/cm^3$
b)
r, cm
r, cm
r, cm

Fig 9

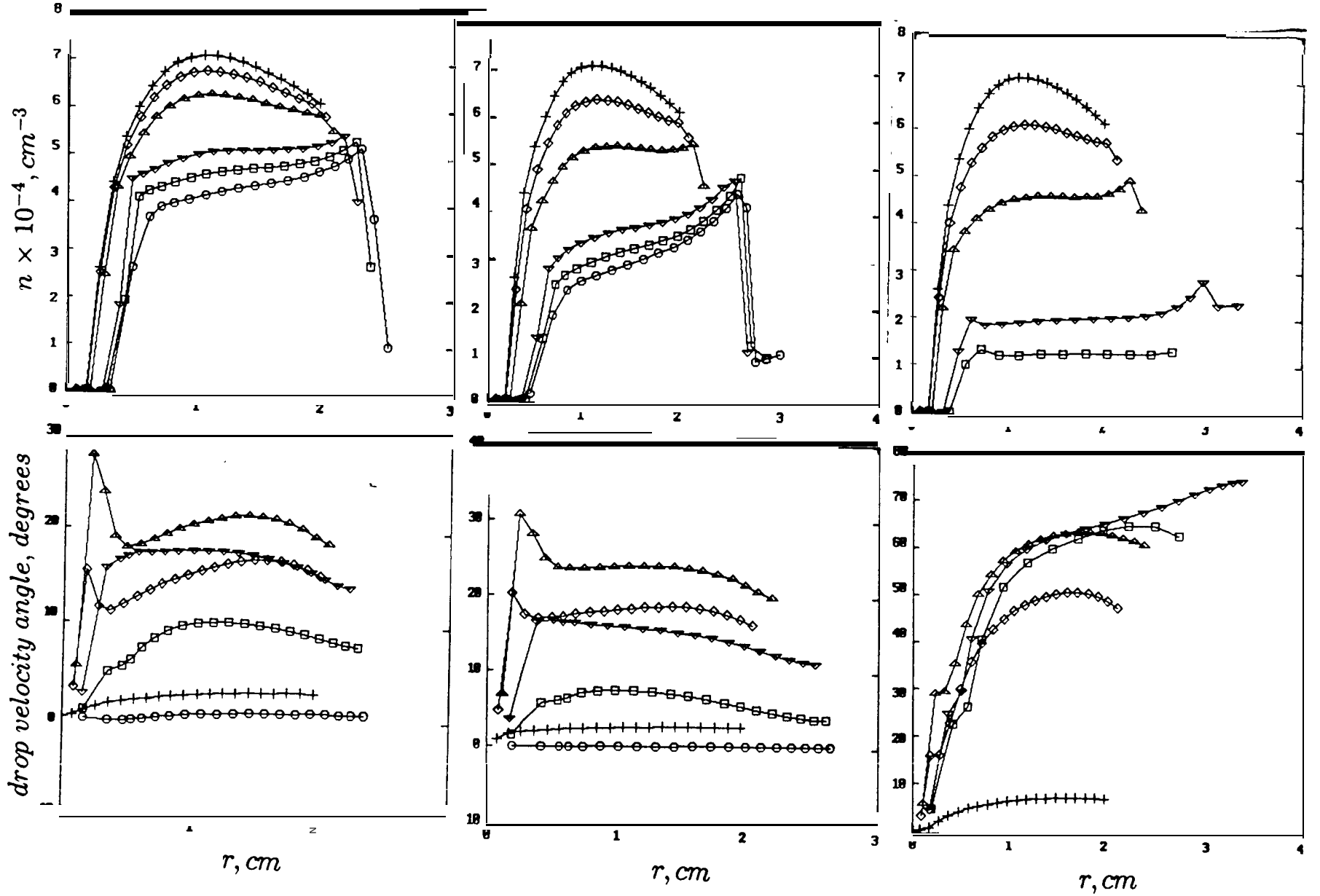

(a) (b) c)

01/24

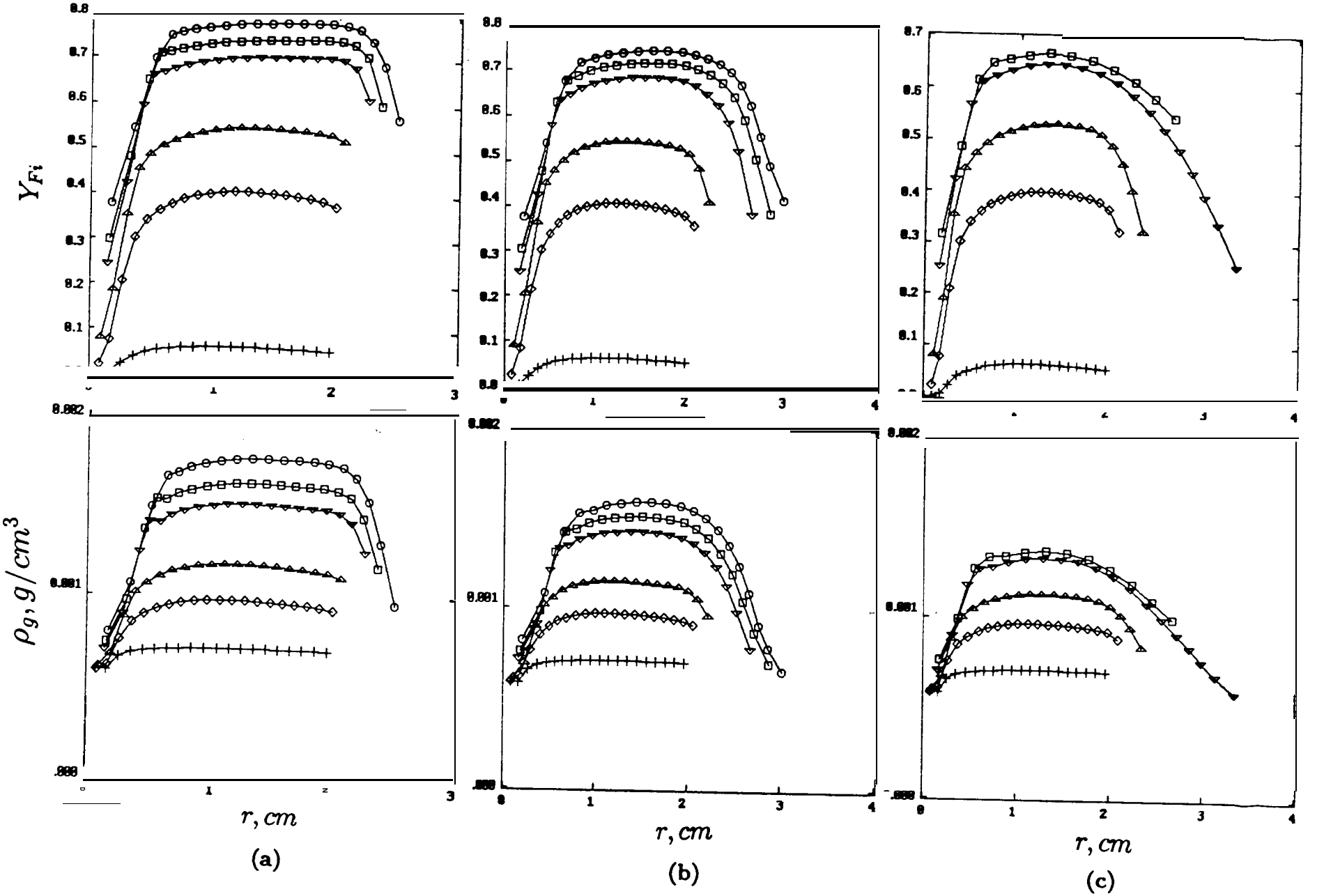
Y_{Fi}
$\rho_g, g/cm^3$
r, cm
(a)
(b)
(c)

Fig 12

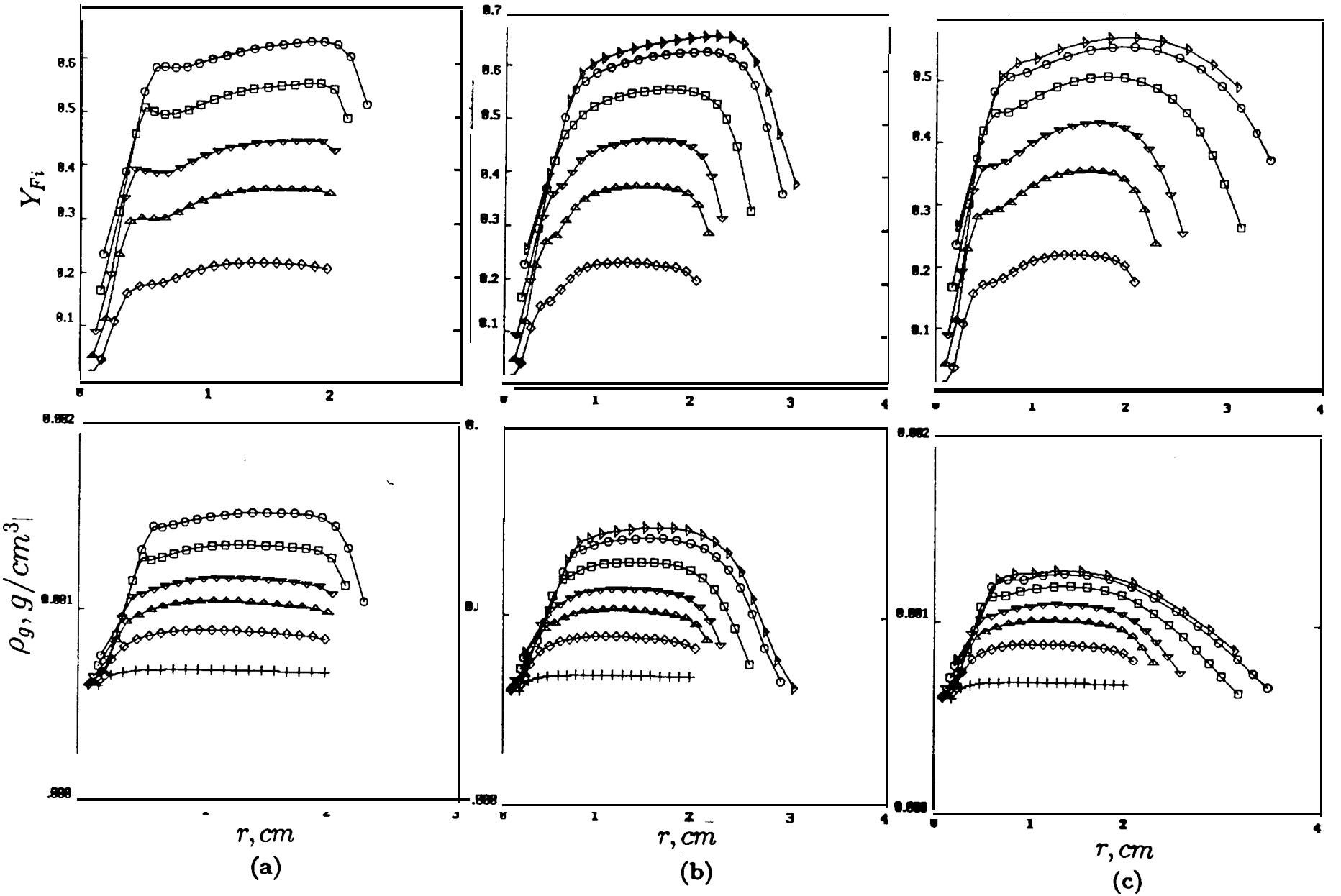

Fig 13

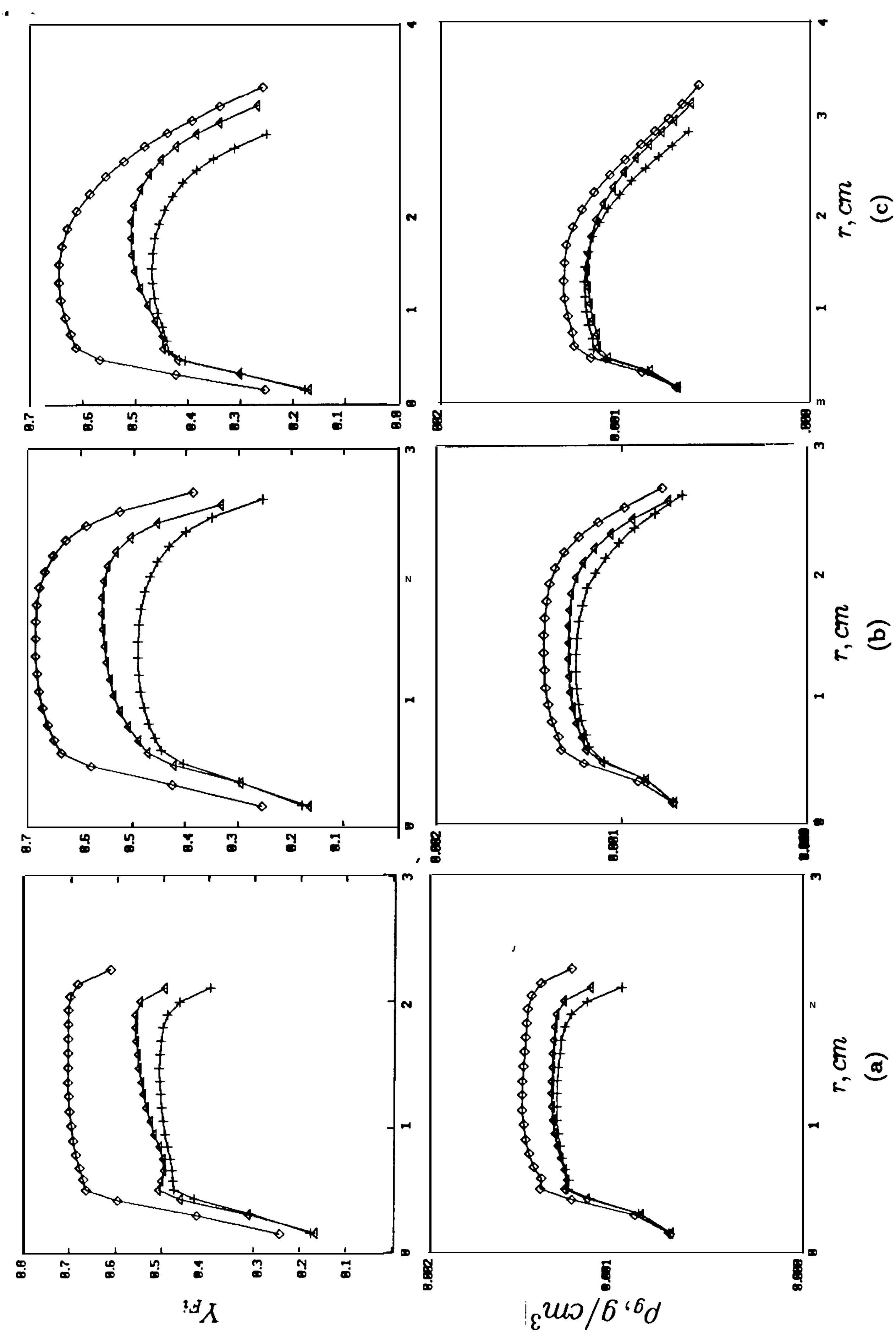

Fig. 14